

Article

Energy Storage Analysis of UIO-66 and Water Mixed Nanofluids: An Experimental and Theoretical Study

Yingjie Zhou ¹, Qibin Li ^{2,*} and Qiang Wang ^{2,*}

¹ College of Computer Science, Sichuan University, Chengdu 610065, China

² Key Laboratory of Low-grade Energy Utilization Technologies & Systems, Ministry of Education, College of Energy and Power Engineering, Chongqing University, Chongqing 400044, China

* Correspondence: qibinli@cqu.edu.cn (Q.L.); wangqiang870609@163.com (Q.W.);
Tel.: +86-0185-8050-4513 (Q.L.)

Received: 4 May 2019; Accepted: 28 June 2019; Published: 30 June 2019



Abstract: The thermal energy storage properties of a working fluid can be modified by the exothermic and endothermic adsorption and desorption of fluid molecules in the micro/nanoporous materials. In this study, thermogravimetric (TG) analysis experiments and molecular simulations (molecular dynamics, MD, and grand canonical Monte Carlo, GCMC) were employed to examine the thermal energy storage properties of the UIO-66 metal organic framework material, UIO-66/H₂O nanofluids and pure water. Our results showed that the molecular simulation calculations were, in principle, consistent with the obtained experimental data. The thermal energy storage performance of UIO-66/H₂O nanofluids was enhanced with the increase in the UIO-66 mass fraction. In addition, the differences between the simulation calculations and experimental results could be mainly ascribed to the different structures of UIO-66 and the evaporation of fluid samples. Furthermore, this work indicated that molecular simulations contributed to developing novel working pairs of metal organic heat carriers (MOHCs).

Keywords: nanofluid; adsorption; energy storage; H₂O; UIO-66

1. Introduction

The energy crisis is one of today's most concerning issues and can be ascribed to the devastating consumption of fossil fuels over the past few centuries. Typically, thermodynamic cycles have become the main approach used to conserve energy since the industrial revolution [1], while the working fluid is the energy carrier in the thermodynamic cycles. Therefore, the efficiency of thermodynamic cycles can be enhanced by employing a working fluid with good thermophysical properties [2–4]. Notably, mixing the working fluid with other materials is a promising way to modify the thermophysical properties of the basic working fluid. It has been extensively reported that nanofluids and working fluid mixed with nanoparticles possess superior thermal conductivity to that of pure fluid [5–11]. In particular, nanofluids have been applied in energy storage systems to enhance the thermal conductivity of the energy storage materials [12–15].

Nanofluids containing micro/nanoporous materials can be applied in energy storage since additional energy is required to desorb the working fluid molecules from the pores during evaporation. As a result, the nanofluid will release excess heat due to the exothermic adsorption of working fluid molecules into the micro/nanoporous materials during condensation [16]. Thus, more power is generated from the thermodynamic cycle with this type of nanofluid. Xu et al. [17–19] investigated the conversion among thermal energy, mechanical energy and electrical energy in the water/carbon nanotube nanofluid, and their results suggested that the energy density in the nanofluids system was higher than that in pure water. Furthermore, McGrail et al. [20] tested the thermal energy storage

properties of refrigerants/metal organic frameworks (MOFs) in which nanofluids served as the metal organic heat carriers (MOHCs) and revealed that R123 MOHC had produced 15% more power than that of the basic fluid. Therefore, nanofluids containing micro/nanoporous materials have great application potential in the field of energy.

MOFs [21] are a subclass of coordination polymers which consist of metal ions (or clusters) coordinated to the organic ligands. In addition, MOFs possess nanoscale porous structures, along with a high specific surface area for adsorption, separation and catalysis [22–24]. Henninger et al. [25] had examined the feasibility of several MOFs as the adsorbents for low-temperature heating and cooling applications. Rezk et al. [26] investigated the adsorption characteristics of water in HKUST-1 and MIL-100 MOFs. Their results suggested that HKUST-1 performed much better than silica gel, which could considerably improve the application of MOFs in adsorption refrigeration, heat pump and thermal storage. Elsayed et al. [27] analyzed the adsorption property of water in Ni-MOF-74 and proved its feasibility for thermal energy storage. Moreover, Zheng et al. [28] reported the adsorption isotherms of water and R134a in the moisture-stable Ni-MOF-74, and their results suggested that the adsorption patterns differed remarkably for the hydrophobic/hydrophilic pores.

Molecular simulation (MS) [29] was employed to unveil the mechanism of the fluid–solid interaction in MOF structures, which can be attributed to its superiority regarding nanoscale investigations [30]. For instance, Sun et al. [31] simulated the diffusion and adsorption properties of n-hexane and cyclohexane in Ni\DOBDc MOF using molecular dynamics (MD) and showed that the attractive interaction between n-hexane and Ni\DOBDc was stronger than that of cyclohexane. In addition, Annapureddy et al. [32] investigated the adsorption mechanism of various gases, R12, R143a and methane in MOFs by means of MD and grand canonical Monte Carlo (GCMC) techniques.

Working fluid and MOFs have diverse and abundant structures and components; therefore, the properties of MOHCs should be further investigated. Typically, among the various MOF structures, UIO-66 [33] demonstrates exceptional stability and good adsorption properties. Meanwhile, water molecules display considerable adsorption enthalpies in MOFs [34]. Consequently, the energy storage properties of UIO-66 and water mixed with nanofluids were analyzed using the experiments and MS calculations detailed in this study.

2. Experimental and Computational Methods

2.1. Experimental Methods

In this study, UIO-66 was synthesized based on the description by Katz et al. [35] after certain modification with reference to the method by Cao et al. [36]. Typically, dimethyl formamide (DMF) (Chongqing Chuandong Chemical Reagent, China AR, 99%), methanol (Chongqing Chuandong Chemical Reagent, China AR, 99%), ZrCl₄ (Macklin, 100 g, 98%), benzenedicarboxylic acid (H₂BDC) (Adamas, 99%), and HCl (Chongqing Chuandong Chemical Reagent, China AR, 98%) were the raw materials for synthesis. In brief, ZrCl₄ and H₂BDC were dissolved in the mixed solution of DMF and HCl under stirring at first. Then, the mixture was transferred into the reaction vessel with a Teflon lining to react at 393 K for 24 h. Afterwards, the mixture was cooled to room temperature, and the product was washed with DMF and methanol repeatedly. Afterwards, the UIO-66 product was dried at 393 K for 12 h [37].

Next, the synthesized UIO-66 powder was mixed with ultrapure water under ultrasonic oscillation (Ultrasonic Cell Disruptor, SCIENTZ-IIID) for 30 min, so as to produce the water/UIO-66 nanofluids with 1% and 3% wt of UIO-66. Subsequently, the nanofluids (with 1% and 3% wt of UIO-66) and ultrapure water were tested by thermogravimetric analysis (TG-DSC, STA-409PC) from room temperature (298.32 K) to 360 K, at a heating rate of 10 K/min, under a nitrogen atmosphere with a flow rate of 15 mL/min. Additionally, the UIO-66 powder was tested in the TG-DSC system from room temperature (297.94 K) to 480 K at a heating rate of 20 K/min under a nitrogen atmosphere at a flow rate of 15 mL/min. The experiments were repeated four times for 10 mg of each sample.

2.2. Simulation Details

Theoretically, the calculations of energy storage properties of MOHCs (Δh_{MOHCs}) during the endothermic process should be performed on Formula [20]:

$$\Delta h_{\text{MOHCs}} = (1 - x) \Delta h_{\text{Fluid}} + x \left(\int_{T_0}^{T_1} C_p dT \right)_{\text{MOFs}} + x \cdot \Delta h_{\text{desorption}}, \quad (1)$$

where Δh_{Fluid} is the enthalpy change of pure working fluid, $\left(\int_{T_0}^{T_1} C_p dT \right)_{\text{MOFs}}$ represents the thermodynamic energy change in MOF nanoparticles when the temperature changes from T_0 to T_1 , $\Delta h_{\text{desorption}}$ stands for the desorption heat of fluid in MOF nanoparticles, while x indicates the mass fraction of MOF nanoparticles in MOHCs.

Research on the thermophysical properties of pure species, especially water, is mature, so the Δh_{Fluid} of water from T_0 to T_1 can be obtained through experimental and theoretical methods. In this study, the Δh_{Fluid} of water was obtained from the National Institute of Standards and Technology (NIST [38]), while the properties of MOFs should be further explored for their various structures and components. As aforementioned, MS had been proven to be a powerful tool to investigate the properties of novel nanomaterials. Thus, the thermodynamic energy change in UIO-66 was calculated by MD simulations, and the desorption heat of H_2O in UIO-66 was measured through GCMC simulations using the Materials Studio software [39] on a Dell Precision Workstation T7910 in our laboratory. In addition, the cut-off distance of simulations was set at 12.5 \AA (10^{-10} m), and periodic boundary conditions were applied in the X, Y and Z axes. The atom–atom interactions in the systems were described by means of the COMPASS force field [40] as follows.

$$\begin{aligned} E = & \sum_b \left[k_2(b - b_0)^2 + k_3(b - b_0)^3 + k_4(b - b_0)^4 \right] \\ & + \sum_\theta \left[k_2(\theta - \theta_0)^2 + k_3(\theta - \theta_0)^3 + k_4(\theta - \theta_0)^4 \right] \\ & + \sum_\phi \left[k_1(1 - \cos \phi) + k_2(1 - \cos 2\phi) + k_3(1 - \cos 3\phi) \right] \\ & + \sum_\chi k_2 \chi^2 + \sum_{b,b'} k(b - b_0)(b' - b'_0) \\ & + \sum_{b,\theta} k(b - b_0)(\theta - \theta_0) + \sum_{b,\phi} (b - b_0)(k_1 \cos \phi + k_2 \cos 2\phi + k_3 \cos 3\phi) \\ & + \sum_{\theta,\phi} (\theta - \theta_0)(k_1 \cos \phi + k_2 \cos 2\phi + k_3 \cos 3\phi) \\ & + \sum_{b,\theta} k(\theta - \theta_0)(\theta' - \theta'_0) + \sum_{\theta,\theta,\phi} k(\theta - \theta_0)(\theta' - \theta'_0) \cos \phi \\ & + \sum_{i>j} \frac{q_i q_j}{r_{ij}} + \sum \varepsilon_{ij} \left[2 \left(\frac{r_{ij}^0}{r_{ij}} \right)^9 - 3 \left(\frac{r_{ij}^0}{r_{ij}} \right)^6 \right] \end{aligned} \quad (2)$$

Clearly, this function consists of the valence terms and the nonbonding interaction terms, among which, the bond (b), angle (θ), torsion angle (ϕ), out of plane angle (χ), and the combinations of two or three internal coordinates, are the valence terms. Meanwhile, the LJ 9-6 function and Coulombic function are the van der Waals terms, whereas the electrostatic interaction is the nonbonding interaction term. In this work, the charges in UIO-66 and water were assigned based on the COMPASS force field, and the structures and systems were kept electronically neutral. Besides, the Ewald summation method was also employed to correct the long-range Coulomb interactions.

2.2.1. MD Details

Notably, the structure of UIO-66, a 3D-framework comprising of one main octahedral cage and eight tetrahedral subordinate cages, in which the octahedral Zr is connected to twelve organic ligands (p-phthalic acid) [33]. As shown in Figure 1, the $4 \times 4 \times 4$ unit cells of UIO-6 (including 192 Zr atoms, 1536 C atoms, 896 H atoms and 1024 O atoms) were built in the simulation model. The original crystal

structure was obtained from the Cambridge Crystallographic Data Centre (CCDC). Afterwards, the model was simulated by MD at 300, 320, 340, 360, 380, 400, and 420 K in the canonical (NVT) ensemble, with a timestep of 0.01 fs (10^{-15} s). Moreover, the temperature was controlled using the Berendsen thermostat, and the computation of thermodynamic energy for the model lasted for 200 ps (10^{-12} s) after a 500 ps simulation was carried out for equilibration.

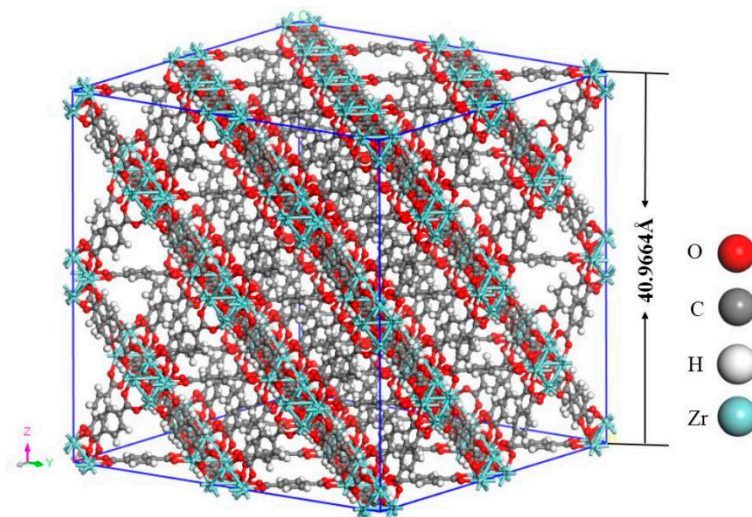


Figure 1. The $4 \times 4 \times 4$ unit cells of UIO-6.

2.2.2. GCMC Details

The adsorption isotherms of H_2O in the UIO-66 nanoparticles, the model in Figure 1, were simulated by means of GCMC from 300 to 360 K at an interval of 5 K. The pressure was set from 1 to 200 kPa with 10 data points. At the same time, the fugacity was calculated using the Peng–Robinson equation, and the equilibration time was 50,000 cycles for each point of the adsorption isotherm, while the statistical time was 100,000 cycles. Therefore, the desorption heat could be computed based on the adsorption isotherms. More details of the simulations are described elsewhere [41].

3. Results and Discussion

3.1. Thermodynamic Energy of UIO-66

The relationship of thermodynamic energy of UIO-66 with the temperature change was plotted in Figure 2. Theoretically, the thermodynamic energy change per temperature unit was the C_p , which represented the slope of the curve in Figure 2. The thermodynamic energy of UIO-66 was linearly increased when the temperature had increased from 0 to 120 K in MD, which was from 300 to 420 K in practice. The UIO-66 measured by MD was the perfect structure, as a result, it could be inferred that the thermodynamic energy of UIO-66 would be linearly increased with the increase in temperature until the material experienced the phase transition during the simulations. Here, the C_p of UIO-66 measured by MD was about 1.74 kJ/kg·K, and the thermodynamic energy of UIO-66 measured by TG-DSC was also linearly elevated when the temperature difference was increased from 0 K to 90 K. In the meantime, the C_p was about 1.27 kJ/kg·K, which was lower than that computed by MD, since the defects and impurities in the UIO-66 experimental sample could not be avoided in the experiment. Noteworthy, our results measured by TG-DSC were consistent with the experimental results of MOF structures presented by Jiang et al. [42] and Lv et al. [43]. Afterwards, the C_p started to enlarge as the temperature difference was increased to over 90 K. This tendency was in agreement with those of the reported papers [20,44] that experimentally investigated the thermal properties of MOFs.

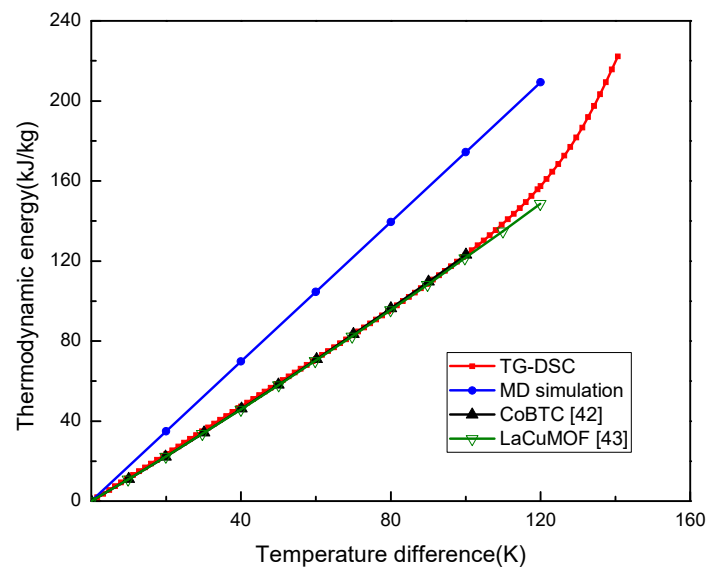


Figure 2. Thermodynamic energy of UIO-66 measured by MD and TG-DSC.

3.2. Thermal Energy Storage Properties of the $H_2O/UIO-66$ Nanofluids

The enthalpy difference represents the thermal energy storage capacity of the fluid sample. Afterwards, the enthalpy differences in water and UIO-66/ H_2O nanofluids (1% wt and 3% wt) were theoretically calculated based on Equation (1). As shown in Figure 3, the enthalpy differences in the investigated fluid samples increased linearly when the temperature was increased from 300 K to 360 K. MOFs accounted for a low mass fraction in UIO-66; therefore, the shape of the enthalpy difference curves of MOHCs was mainly dependent on the enthalpy difference of the pure fluid. The calculation results denoted that the thermal energy storage capacity of pure water could be strengthened by adding the UIO-66 powders. Specifically, the energy storage capacity of UIO-66/ H_2O nanofluids (1% wt) was about 2% higher than that of pure water, and that of UIO-66/ H_2O nanofluids (3% wt) was about 6% higher than that of pure water, indicating that more energy could be stored in the UIO-66/water nanofluid when more UIO-66 powders were added.

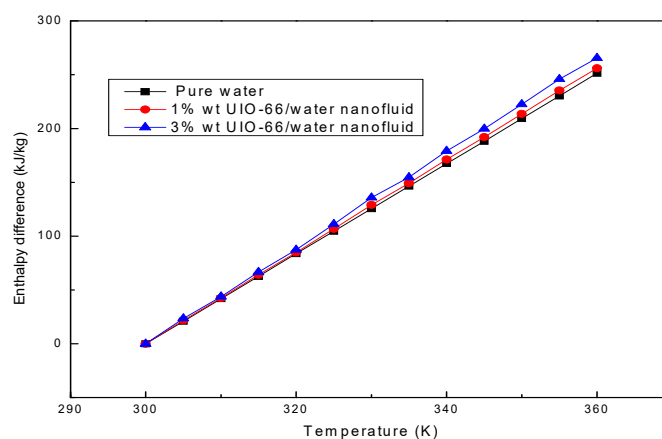


Figure 3. The enthalpy differences of water and UIO-66/ H_2O nanofluids assessed by theoretical calculation.

The enthalpy differences of ultrapure water and UIO-66/ H_2O nanofluids (1% wt and 3% wt) were measured by TG-DSC, as displayed in Figure 4. The experiments also showed that the UIO-66/water nanofluids had superior thermal energy storage capacities upon the increase in the mass fraction of UIO-66. Evidently, the enhancement ratio of the energy storage capacity for UIO-66/ H_2O nanofluids was reduced with the increase in temperature. However, the slope of the enthalpy difference curves

was enhanced with the increase in temperature, since fluid evaporation was boosted as the experiments proceeded. Water evaporation would remove energy in the form of heat from the tested sample, and the latent heat during the evaporation was larger than that of the sensible heat. As a result, more energy would be required to maintain the heating rate of the TG-DSC. Consequently, the enthalpy difference during the experiments would experience a sharp increase at high temperature. As shown in Figure 5, the evaporation rates of fluid samples followed the order of ultrapure water > 1% wt UIO-66/water nanofluid > 3% wt UIO-66/water nanofluid. This is because the water had evaporated and the UIO-66 particles were left in the samples.

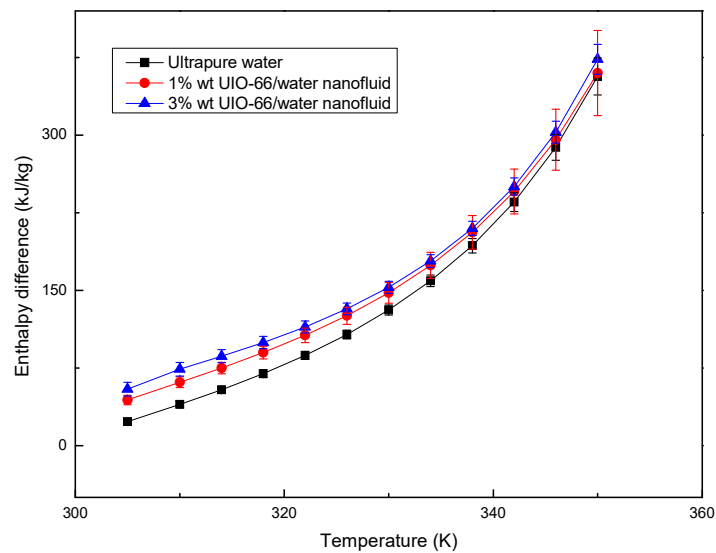


Figure 4. Enthalpy difference of ultrapure water and UIO-66/H₂O nanofluids measured by TG-DSC.

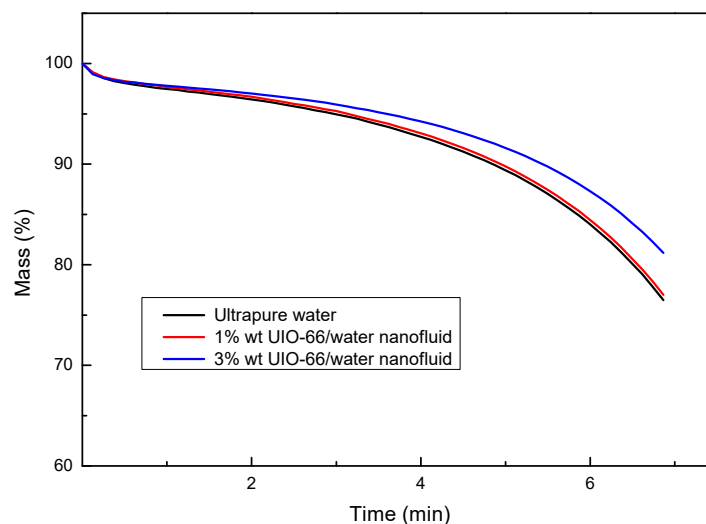


Figure 5. Mass changes of ultrapure water and UIO-66/H₂O nanofluids measured by TG-DSC.

Two main reasons were responsible for the different energy storage capacities between the simulations and experimental results. On one hand, the UIO-66 in the simulation was the perfect structure, while that which was used in the experiments had a defective structure. On the other hand, the fluid would evaporate during the experiments, while the fluid samples in the simulations were ideal and would not evaporate, which enabled the calculation of energy at different temperatures. Nonetheless, to save costs, MS can be used to develop and design novel working pairs of MOHCs with excellent properties through calculations using various refrigerants and MOFs. Additionally,

the simulation model can also be extended and optimized in other MOHCs with refrigerants in our future work.

4. Conclusions

In this study, the thermal energy storage capacities of UIO-66 powders, UIO-66/H₂O nanofluids and pure water are investigated using TG-DSC experiments and MS calculations, respectively. The thermodynamic energy changes of the UIO-66 powders measured in the experiments provided a good match with the reported data. Both MD and the experiments indicate that the thermodynamic energy change in UIO-66 increased with the increase in temperature. The differences between the simulations and experimental results can be ascribed to the different structures of tested samples in the simulations and experiments. Furthermore, the results of both methods suggest that the thermal energy storage capacity of UIO-66/H₂O nanofluids is enhanced with the increase in the mass fraction of UIO-66. MOHCs have various and abundant working pairs; consequently, this work has provided an efficient and low-cost simulation approach to investigate the energy storage properties of novel MOHCs.

Author Contributions: Conceptualization, Q.L. and Q.W.; methodology, Y.Z. and Q.L.; formal analysis, Y.Z., Q.L. and Q.W.; resources, Q.L.; data curation, Y.Z., Q.L. and Q.W.; writing—original draft preparation, Y.Z., Q.L. and Q.W.; writing—review and editing, Y.Z., Q.L. and Q.W.; visualization, Q.W.; supervision, Q.L.; project administration, Q.L.; funding acquisition, Q.L.

Funding: This work is supported by the National Natural Science Foundation of China (Nos. 51876015, 51506013), Fundamental Research Funds for the Central Universities of China (No. 2018CDXYDL0001).

Acknowledgments: The authors would like to acknowledge the colleagues from the Key Laboratory of Low-grade Energy Utilization Technologies & Systems, Ministry of Education for their perspectives and suggestions related to data collection and statistical analysis.

Conflicts of Interest: The authors declare no conflict of interest.

References

1. Morales-Rodriguez, R. *Thermodynamics-Fundamentals and Its Application in Science*; InTech: Rijeka, Croatia, 2012.
2. Zhang, C.; Liu, C.; Xu, X.; Li, Q.; Wang, S.; Chen, X. Effects of superheat and internal heat exchanger on thermo-economic performance of organic Rankine cycle based on fluid type and heat sources. *Energy* **2018**, *159*, 482–495. [[CrossRef](#)]
3. Liu, X.; Ye, Z.; Bai, L.; He, M. Performance comparison of two absorption-compression hybrid refrigeration systems using R1234yf/ionic liquid as working pair. *Energy Convers. Manag.* **2019**, *181*, 319–330. [[CrossRef](#)]
4. Liu, X.; Zhu, C.; Yang, F.; Su, C.; He, M. Experimental and correlational study of isobaric molar heat capacities of fatty acid esters: Ethyl nonanoate and ethyl dodecanoate. *Fluid Phase Equilibria* **2019**, *479*, 47–51. [[CrossRef](#)]
5. Eastman, J.A.; Choi, S.U.S.; Li, S.; Yu, W.; Thompson, L.J. Anomalously increased effective thermal conductivities of ethylene glycol-based nanofluids containing copper nanoparticles. *Appl. Phys. Lett.* **2001**, *78*, 718–720. [[CrossRef](#)]
6. Keblinski, P.; Phillpot, S.R.; Choi, S.U.S.; Eastman, J.A. Mechanisms of heat flow in suspensions of nano-sized particles (nanofluids). *Int. J. Heat Mass Transf.* **2002**, *45*, 855–863. [[CrossRef](#)]
7. Ho, C.J.; Gao, J.Y. Preparation and thermophysical properties of nanoparticle-in-paraffin emulsion as phase change material. *Int. Commun. Heat Mass Transf.* **2009**, *36*, 467–470. [[CrossRef](#)]
8. Yang, X.; Li, S.; Huang, H.; Li, J.; Kobayashi, N.; Kubota, M. Effect of carbon nanoadditives on lithium hydroxide monohydrate-based composite materials for low temperature chemical heat storage. *Energies* **2017**, *10*, 664. [[CrossRef](#)]
9. Wang, J.; Zhou, S.; Zhang, Z.; Yurchenko, D. High-performance piezoelectric wind energy harvester with Y-shaped attachments. *Energy Convers. Manag.* **2019**, *181*, 645–652. [[CrossRef](#)]
10. Sohail, A.; Fatima, M.; Ellahi, R.; Akram, K.B. A video graphic assessment of ferrofluid during magnetic drug targeting: An application of artificial intelligence in nanomedicine. *J. Mol. Liq.* **2019**, *285*, 47–57. [[CrossRef](#)]
11. Rashidi, S.; Akar, S.; Bovand, M.; Ellahi, R. Volume of fluid model to simulate the nanofluid flow and entropygeneration in a single slope solar still. *Renew. Energy* **2018**, *115*, 400–410. [[CrossRef](#)]

12. Yang, X.; Xiong, T.; Dong, J.L.; Li, W.X.; Wang, Y. Investigation of the dynamic melting process in athermal energy storage unit using a helical coil heat exchanger. *Energies* **2017**, *10*, 1129. [[CrossRef](#)]
13. Hussian, M.I.; Kim, J.; Kim, J. Nanofluid-powered dual-fluid photovoltaic/thermal (PV/T) system: Comparative numerical study. *Energies* **2019**, *12*, 775. [[CrossRef](#)]
14. Cho, S.; Kim, J.; Kim, J. Optimal operation parameter estimation of energy storage for frequency regulation. *Energies* **2019**, *12*, 1782. [[CrossRef](#)]
15. Zeeshan, A.; Shehzad, N.; Abbas, T.; Ellahi, R. Effects of radiative electro-magneto hydrodynamics diminishing internal energy of pressure-driven flow of titanium dioxide-water nanofluid due to entropy generation. *Entropy* **2019**, *21*, 236. [[CrossRef](#)]
16. Chen, X.; Xu, B.; Liu, L. Nanoscale fluid mechanics and energy conversion. *Appl. Mech. Rev.* **2014**, *66*, 050803. [[CrossRef](#)]
17. Xu, B.; Qiao, Y.; Chen, X. Mitigating impact/blast energy via a novel nanofluidic energy capture mechanism. *J. Mech. Phys. Solids* **2014**, *62*, 194–208. [[CrossRef](#)]
18. Xu, B.; Chen, X. Liquid flow-induced energy harvesting in carbon nanotubes: A molecular dynamics study. *Phys. Chem. Chem. Phys.* **2013**, *15*, 1164–1168. [[CrossRef](#)]
19. Xu, B.; Liu, L.; Lim, H.; Qiao, Y.; Chen, X. Harvesting energy from low-grade heat based on nanofluids. *Nano Energy* **2012**, *1*, 805–811. [[CrossRef](#)]
20. McGrail, B.P.; Thallapally, P.K.; Blanchard, J.; Nune, S.K.; Jenks, J.J.; Dang, L.X. Metal-organic heat carrier nanofluids. *Nano Energy* **2013**, *2*, 845–855. [[CrossRef](#)]
21. James, S.L. Metal-organic frameworks. *Chem. Soc. Rev.* **2003**, *32*, 276–288. [[CrossRef](#)]
22. Murray, L.J.; Dincă, M.; Long, J.R. Hydrogen storage in metal-organic frameworks. *Chem. Soc. Rev.* **2009**, *38*, 1294–1314. [[CrossRef](#)] [[PubMed](#)]
23. Li, J.R.; Sculley, J.; Zhou, H.C. Metal-organic frameworks for separations. *Chem. Rev.* **2012**, *112*, 869–932. [[CrossRef](#)] [[PubMed](#)]
24. Liu, J.; Thallapally, P.K.; McGrail, B.P.; Brown, D.R.; Liu, J. Progress in adsorption-based CO₂ capture by metal-organic frameworks. *Chem. Soc. Rev.* **2012**, *41*, 2308–2322. [[CrossRef](#)] [[PubMed](#)]
25. Henninger, S.K.; Habib, H.A.; Janiak, C. MOFs as adsorbents for low temperature heating and cooling applications. *J. Am. Chem. Soc.* **2009**, *131*, 2776–2777. [[CrossRef](#)] [[PubMed](#)]
26. Rezk, A.; Al-Dadah, R.; Mahmoud, S.; Elsayed, A. Characterisation of metal organic frameworks for adsorption cooling. *Int. J. Heat Mass Transf.* **2012**, *55*, 7366–7374. [[CrossRef](#)]
27. Elsayed, A.; Elsayed, E.; Al-Dadah, R.; Mahmoud, S.; Elshaer, A.; Kaialy, W. Thermal energy storage using metal-organic framework materials. *Appl. Energy* **2017**, *186*, 509–519. [[CrossRef](#)]
28. Zheng, J.; Vemuri, R.S.; Estevez, L.; Koech, P.K.; Varga, T.; Camaioni, D.M.; Blake, T.A.; McGrail, B.P.; Motkuri, R.K. Pore-engineered metal-organic frameworks with excellent adsorption of water and fluorocarbon refrigerant for cooling applications. *J. Am. Chem. Soc.* **2017**, *139*, 10601–10604. [[CrossRef](#)]
29. Frenkel, D.; Smit, B. *Understanding Molecular Simulation: From Algorithms to Applications*, 2nd ed.; Academic Press: New York, NY, USA, 2002.
30. Zhang, N.; Huo, J.; Yang, B.; Ruan, X.; Zhang, X.; Bao, J.; Qi, W.; He, G. Understanding of imidazolium group hydration and polymer structure for hydroxide anion conduction in hydrated imidazolium-g-PPO membrane by molecular dynamics simulations. *Chem. Eng. Sci.* **2018**, *192*, 1167–1176. [[CrossRef](#)]
31. Sun, X.; Wick, C.D.; Thallapally, P.K.; McGrail, B.P.; Dang, L.X. Computational study of hydrocarbon adsorption in metal-organic framework Ni₂(dhtp). *J. Phys. Chem. B* **2011**, *115*, 2842–2849. [[CrossRef](#)]
32. Annapureddy, H.V.R.; Motkuri, R.K.; Nguyen, P.T.M.; Truong, T.B.; Thallapally, P.K.; McGrail, B.P.; Dang, L.X. Computational studies of adsorption in metal organic frameworks and interaction of nanoparticles in condensed phases. *Mol. Simul.* **2014**, *40*, 571–584. [[CrossRef](#)]
33. Cmarik, G.E.; Kim, M.; Cohen, S.M.; Walton, K.S. Tuning the adsorption properties of UiO-66 via ligand functionalization. *Langmuir* **2012**, *28*, 15606–15613. [[CrossRef](#)] [[PubMed](#)]
34. Chaemchuen, S.; Xiao, X.; Klomkliang, N.; Yusubov, M.S.; Verpoort, F. Tunable Metal—Organic Frameworks for Heat Transformation Applications. *Nanomaterials* **2018**, *8*, 661. [[CrossRef](#)] [[PubMed](#)]
35. Katz, M.J.; Brown, Z.J.; Colon, Y.J.; Siu, P.W.; Scheidt, K.A.; Snurr, R.Q.; Hupp, J.T.; Farha, O.K. A facile synthesis of UiO-66, UiO-67 and their derivatives. *Chem. Commun.* **2013**, *49*, 9449–9451. [[CrossRef](#)] [[PubMed](#)]
36. Cao, Y.; Zhao, Y.; Lv, Z.; Song, F.; Zhong, Q. Preparation and enhanced CO₂ adsorption capacity of UiO-66/graphene oxide composites. *J. Ind. Eng. Chem.* **2015**, *27*, 102–107. [[CrossRef](#)]

37. Yang, J.J.; Ding, Y.D.; Liao, Q.; Zhu, X.; Liu, Q.W. Influence of processing conditions on compressive strength and CO₂ adsorption of UiO-66 pellets, IHTC16-22457. In Proceedings of the International Heat Transfer Conference, Beijing, China, 10–15 August 2018.
38. NIST. Available online: <http://webbook.nist.gov/chemistry/fluid/> (accessed on 1 June 2018).
39. Accelrys, I. *Materials Studio*; Accelrys Software Inc.: San Diego, CA, USA, 2010.
40. Sun, H. COMPASS: An ab initio force-field optimized for condensed-phase applications overview with details on alkane and benzene compounds. *J. Phys. Chem. B* **1998**, *102*, 7338–7364. [[CrossRef](#)]
41. Hu, J.; Liu, C.; Li, Q.; Shi, X. Molecular simulation of thermal energy storage of mixed CO₂/IRMOF-1 nanoparticle nanofluid. *Int. J. Heat Mass Transf.* **2018**, *125*, 1345–1348. [[CrossRef](#)]
42. Jiang, C.; Song, L.; Zhang, J.; Sun, L.; Xu, F.; Li, F.; Jiao, Q.; Sun, Z.; Xing, Y.; Du, Y.; et al. Thermodynamic properties and heat capacities of Co (BTC)1/3 (DMF) (HCOO). *J. Therm. Anal. Calorim.* **2010**, *102*, 1087–1093. [[CrossRef](#)]
43. Lv, X.; Tan, Z.; Gao, X.; Zhang, Z.; Yang, L.; Zhao, J.; Sun, L.; Zhang, T. Synthesis and thermodynamic properties of a metal-organic framework: [LaCu₆(μ-OH)₃(Gly)₆im₆](ClO₄)₆. *Thermochimica Acta* **2006**, *450*, 102–104. [[CrossRef](#)]
44. Mu, B.; Walton, K.S. Thermal Analysis and Heat Capacity Study of Metal–Organic Frameworks. *J. Phys. Chem. C* **2011**, *115*, 22748–22754. [[CrossRef](#)]



© 2019 by the authors. Licensee MDPI, Basel, Switzerland. This article is an open access article distributed under the terms and conditions of the Creative Commons Attribution (CC BY) license (<http://creativecommons.org/licenses/by/4.0/>).